ADVANCED OPTICAL MATERIALS
www.advopticalmat.de

Adhesion-Engineering-Enabled "Sketch and Peel" Lithography for Aluminum Plasmonic Nanogaps

Yiqin Chen, Shi Zhang, Zhiwen Shu, Zhaolong Wang, Peng Liu, Chen Zhang, Yasi Wang, Qing Liu, Huigao Duan, and Yanjun Liu*

Aluminum is one of the most significant plasmonic materials for its advantage of low cost, natural abundance, as well as the ultraviolet optical response. However, it is still very challengeable for the fabrication of aluminum plasmonic nanogaps, which greatly limits the applications of aluminum plasmonics considering the essential role of nanogaps for electric field enhancement. Here, the reliable patterning of aluminum plasmonic nanogaps employing a modified "Sketch and Peel" lithography strategy is demonstrated. By introducing a self-assembled monolayer to engineer the surface energy of the substrate, the adhesiveness of the aluminum film outside outline template is significantly decreased to implement the selective peeling process. Besides, the near-infrared Fano resonance in the periodic aluminum heptamers has been first revealed by enabling the strong electric field and plasmon coupling in the aluminum nanostructures with 10 nm scale nanogaps. In addition, surface-enhanced Raman spectroscopy and infrared spectroscopy are also illustrated in the rationally designed aluminum dimers. The present work provides a robust method to obtain aluminum plasmonic nanogaps, which may play an important role on the practical applications of aluminum plasmonics, such as surface-enhanced vibration spectroscopy and nonlinear optics.

1. Introduction

The light energy can be confined in a tiny volume by the plasmon resonance within nanogaps.[1–4] The hotspots from giant nanofocusing effect strongly enhance the interaction between electromagnetic waves and metallic nanoparticles in the near field and amplify both linear and nonlinear phenomena at the single-molecule and single-particle level.[5–9] Choosing an appropriate plasmonic material is significant for different plasmonic applications, usually considering the cost, performance, and process compatibility. Among these materials, silver (Ag) is favored due to its low loss, which supports a strong plasmon resonance in the visible and near-infrared regions.[10] However, the oxidization of Ag in air greatly changes its optical properties, which severely limits the practical use of metallic Ag in plasmonics. In contrast, gold (Au) is a better choice due to its excellent chemical stability, but it suffers from a high intrinsic absorption of photon energy higher than 2.38 eV. As a result, making full use of Au for plasmon-enhanced spectroscopic applications, such as surface-enhanced Raman spectroscopy (SERS) and nonlinear optics in the entire visible region, is difficult.

Compared to Au and Ag, aluminum (Al) is a more promising material for plasmonics, with the merits of oxidation stability superior to that of Ag and the extended optical response ranging from the ultraviolet to visible regime compared to that of Au.[11,12] Nevertheless, the optical loss of Al degrades the nanofocusing effect, which weakens the localization of light field in the nearfield of Al plasmonic nanostructures. For these reasons, tiny plasmonic nanogaps play a significant role in achieving large electric-field enhancement factor for practical applications of Al plasmonics.

From the perspective of fabrication process, the plasmonic nanogaps in metallic structures are intrinsically a type of multiscale configuration, usually ranging from several nanometers to several hundreds of nanometers. To obtain plasmonic nanogaps, electron-beam lithography (EBL) is a key tool due to its advantages of high resolution and accuracy in patterning.[13,14] Traditionally, the whole area of final patterns separated by nanogaps should be fully exposed. However, this patterning strategy has limited resolution and accuracy in gap fabrication due to the large proximity effect caused by electron scattering. Furthermore, this kind of challenge becomes more apparent when fabricating nanogaps in plasmonic nanostructures, which commonly involves metal deposition and lift-off processes.

Dr. Y. Chen, S. Zhang, Z. Shu, Dr. Z. Wang, Dr. P. Liu, C. Zhang, Y. Wang, Q. Liu, Prof. H. Duan
State-Key Laboratory of Advanced Design and Manufacturing for Vehicle Body
College of Mechanical and Vehicle Engineering
Hunan University
Changsha 410082, P. R. China
E-mail: duanhg@hnu.edu.cn
Prof. Y. Liu
Department of Electrical and Electronic Engineering
Southern University of Science and Technology
Shenzhen 518055, P. R. China
The ORCID identification number(s) for the author(s) of this article can be found under https://doi.org/10.1002/adom.201901202.

DOI: 10.1002/adom.201901202

 © 2019 WILEY-VCH Verlag GmbH & Co. KGaA, Weinheim

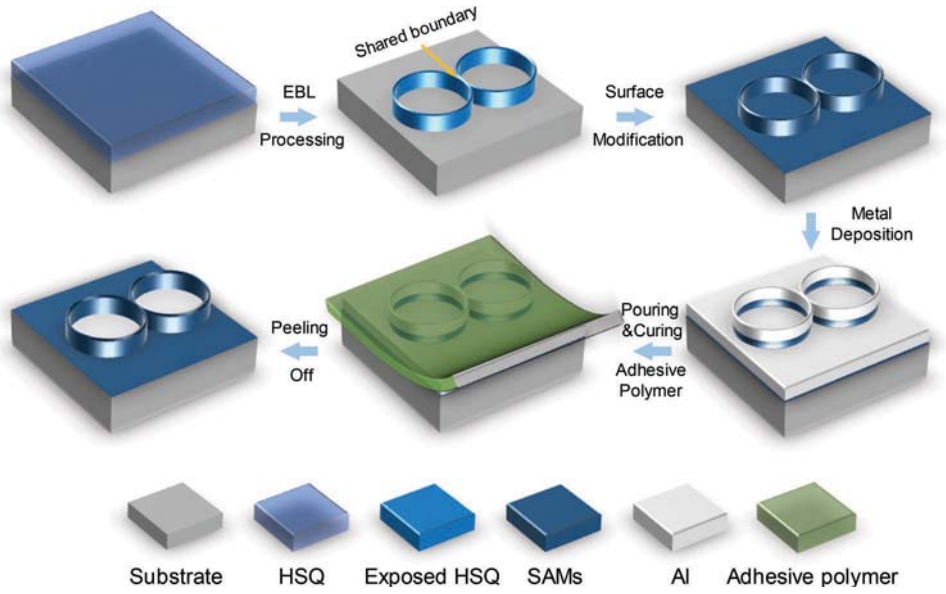

Figure 1. Schematic flow chart of the adhesion-engineering-enabled SPL process for fabricating Al plasmonic nanogaps.

Motivated by this demand on plasmonic nanogap fabrication, we previously developed a "Sketch and Peel" lithography (SPL) process for high-resolution multiscale patterning of plasmonic nanogaps.[15,16] In this process, only the outline template of the target structures is defined, and then, the target structures can be obtained via selective stripping of the deposited metallic film. This method can greatly enhance the patterning efficiency and significantly mitigate the proximity effect for plasmonic nanogaps. However, a basic requirement to implement this process is the strippable behavior of the metallic film from the substrate. For noble metals such as Au and Ag, they have weak adhesion on most optical substrates, such as quartz and sapphire. In contrast, metallic Al has strong adhesion with SiO_2 substrates. The strong adhesion between them limits the applicability of the SPL process for high-resolution patterning of Al plasmonic nanogaps.

In this work, we aim to extend the SPL process for Al plasmonic nanogaps to satisfy the application requirements of Al plasmonics. By introducing a self-assembled antiadhesion monolayer on the substrate, the Al film becomes strippable for implementation of the SPL process, enabling the reliable fabrication of Al plasmonic nanogaps approaching to 10 nanometer scale on a typical SiO_2 optical substrate. The key role of the self-assembled anti-adhesion monolayer on the substrate surface is verified by X-ray photoelectron spectroscopy (XPS) and adhesion energy measurements. Using this modified SPL process, we demonstrate the reliable fabrication of periodic Al heptamers possessing uniform interparticle gaps of ≈12 nm, in which a Fano resonance spectral shape is obtained. Benefiting from the improved resolution, Al bowtie nanostructure with an 8 nm gap is fabricated, showing an appreciable surface-enhanced Raman spectroscopy (SERS) performance at the single-particle level. Meanwhile, a chemical sensor based on the surface-enhanced infrared absorption (SEIRA) shows great enhancement of fingerprint signals from polymethyl methacrylate (PMMA) molecules by the excited resonance of periodic Al fan-shaped antennas with a uniform 15 nm gap. These examples validate the reliability of our modified SPL process in the fabrication of plasmonic Al nanogaps, which will definitely push Al plasmonics toward practical applications.

2. Results and Discussion

The process reported in this work is mainly based on the standard SPL process, we previously developed using the HSQ-based high-resolution EBL process, as shown in **Figure 1**. HSQ resist film is first spin-coated onto a typical optical substrate such as an oxidized silicon wafer or quartz substrate, and then, the HSQ film is patterned by exposing the outline of the target structures. After development, the resultant HSQ outline template is decorated by an self-assembled antiadhesion monolayer via a vapor-phase surface modification process to mitigate the adhesion between Al film and the substrate.[17] This adhesion engineering step is crucial to make the SPL process applicable to fabricate Al structures because it enables metallic Al film to be stripped from the substrate. After Al evaporation, we pour the adhesive polymer onto the as-deposited sample and cure the liquid polymer under the illumination of ultraviolet light. Finally, the inside Al structure is defined on the substrate via stripping the outside Al film. Note that the surface modification of the antiadhesion monolayer is realized by a vapor-based process instead of a wet treatment to avoid collapse of the HSQ nanowall templates.[18]

Based on the above method, some commonly used Al plasmonic structures with nanogaps were fabricated and are shown in **Figure 2**. A smaller nanogap size between Al nanostructures promotes the plasmon coupling effect to modulate their optical properties. For example, the dolmen-shaped nanoantenna in Figure 2a is supposed to have polarization tunability of the transparent window caused by plasmon-induced transmission arising from the strong coupling of different-order

© 2019 WILEY-VCH Verlag GmbH & Co. KGaA, Weinheim

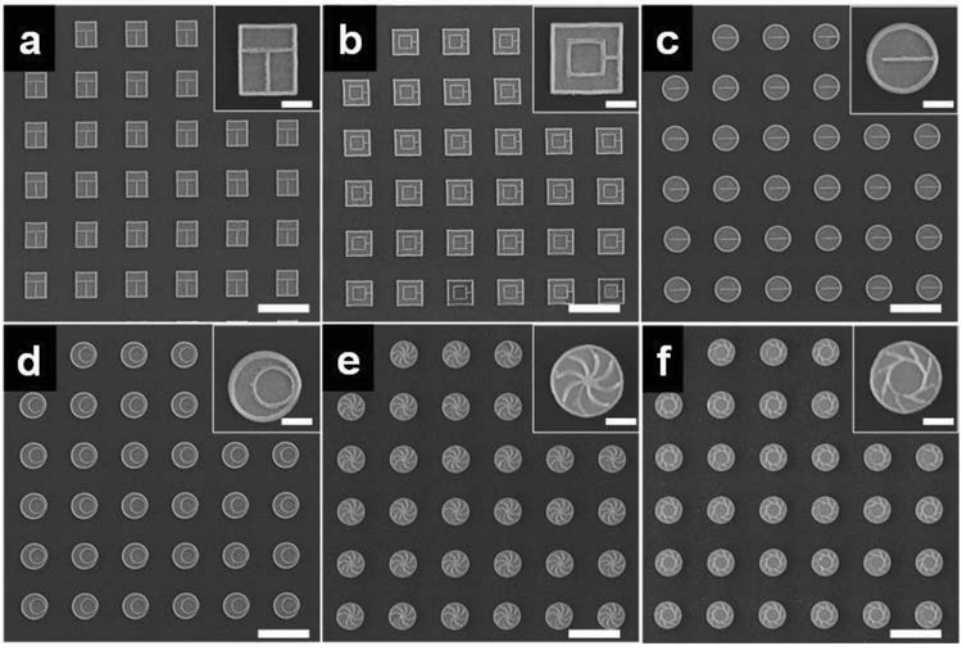

Figure 2. Gallery of Al plasmonic structure arrays with embedded nanogaps of ≈15 nm. a) Periodic dolmen structures. In a dolmen, the top transom nanobrick has a length of 370 nm and a width of 160 nm, and the bottom nanobricks possess identical dimensions of 300 nm in height and 180 nm in width. b) Arrayed Al squares in split boxes. The central square (edge length of 250 nm) is closely encompassed by a split box (edge length of 500 nm). c) Al split disk array. The disk (D = 500 nm) is cut by a radial slit of 450 nm. d) Latticed Al nanoparticles with an asymmetric configuration of an outer nanoscale crescent moon (D = 500 nm) wrapping an inner disk (d = 250 nm) with an eccentricity of 70 nm. e) Al nanopies sliced with equal sinusoidal cutting. The diameter of the pie is 1 µm. f) Al nanodisk (d = 500 nm) in a sliced nanoring (D_{out} = 1 µm). The ring is sliced by part of a sinusoidal curve. All of the white lines in the SEM images present the HSQ outline templates. Scale bar: a–d) 1 µm; e,f) 2 µm. Inset images: a–d) 100 nm; e,f) 200 nm.

resonant modes in the nanobricks.[19] With the SPL process, the Al nanobricks in the dolmen structures were well defined with accurate outlines, high-fidelity corners, and uniform gaps. Figure 2b–d presents asymmetric split rings and split disks. These structures are asymmetrically trimmed by a nanoslit. Such symmetry-breaking structures with smaller nanoslits and interparticle nanogaps are supposed to support stronger Fano resonances.[20] From the SEM images shown in Figure 2b–d, uniform gap and slit with dimensions of ≈15 nm can be obtained. Meanwhile, the high fidelity of the defined structures can be indicated by the sharp corners with a radius of curvature of ≈5 nm, indicating the reliability and precision of the SPL method. Note that HSQ nanowall templates were not removed to avoid damage to Al nanostructures by HF vapor. The existence of HSQ nanowall templates does not affect the main plasmonic applications, such as to enhance spectroscopy and to arouse nonlinear optics, which will be demonstrated in application examples below.

Due to the advantage of the SPL process using a shared boundary to define the nanogaps, the complex plasmonic molecules that are very challenging to fabricate by conventional methods can be well achieved. Figure 2e,f shows kirigami-inspired sliced nanopies and sun-like nanodisks, in which complex shapes with 15 nm gaps between two adjacent particles were defined and well matched the designs. The nanostructure shown in Figure 2e can be used to enhance the conformation sensing of molecules, as demonstrated by Kuzyk et al.[21] Additionally, the nanostructure presented in Figure 2f is supposed to have many more hotspots between the central disk and satellite nanoparticles under the excitation of azimuthal polarization.

The detailed surface treatment process is illustrated in **Figure 3**a. First, the HSQ template is activated when exposed to oxygen plasma, producing siloxyl (Si-OH) group on the surface. The templates are subsequently modified by linkage of SAMs (TFOCS silane, see the details in Experimental Section). The linkage is established between Si-OH groups on the HSQ templates and the trichloro-terminated group of silane molecules.[22] The SAMs were verified by X-ray optoelectronic spectroscopy (XPS), as shown in Figure 3b,c, respectively. These two figures show that the multiple C 1s subpeaks at 285, 291, and 293 eV are consistent with the signals from the skeleton of the C—C chain, $-CF_2-$ and $-CF_3$ groups in the SAM molecule (TFOCS).[23] The specific peak at 287.5 eV is assumed to originate from semi-ionic C—F bonding.[24] Meanwhile, the absence of Cl 2p peaks from the XPS spectrum indicates that the linkage of SAMs on the surface occurs through siloxane bonding via the reaction with the hydroxyl group on the substrate by desorbing chloride atoms. The strong linkage of the SAMs with the substrate guarantees the peeling process.

After adhesion engineering, the adhesiveness between the SiO_2 substrate and Al film was characterized by an adhesion energy test system (as shown in Figure S1, Supporting Information). The dashed blue box inserted in Figure 3d shows that the Al film was easily peeled off from the SAM-modified SiO_2 surface. In contrast, peeling Al film off from the uncoated pristine SiO_2 surface was very difficult. Instead, breakage occurred at the interface between the Al film and the cured adhesive

© 2019 WILEY-VCH Verlag GmbH & Co. KGaA, Weinheim

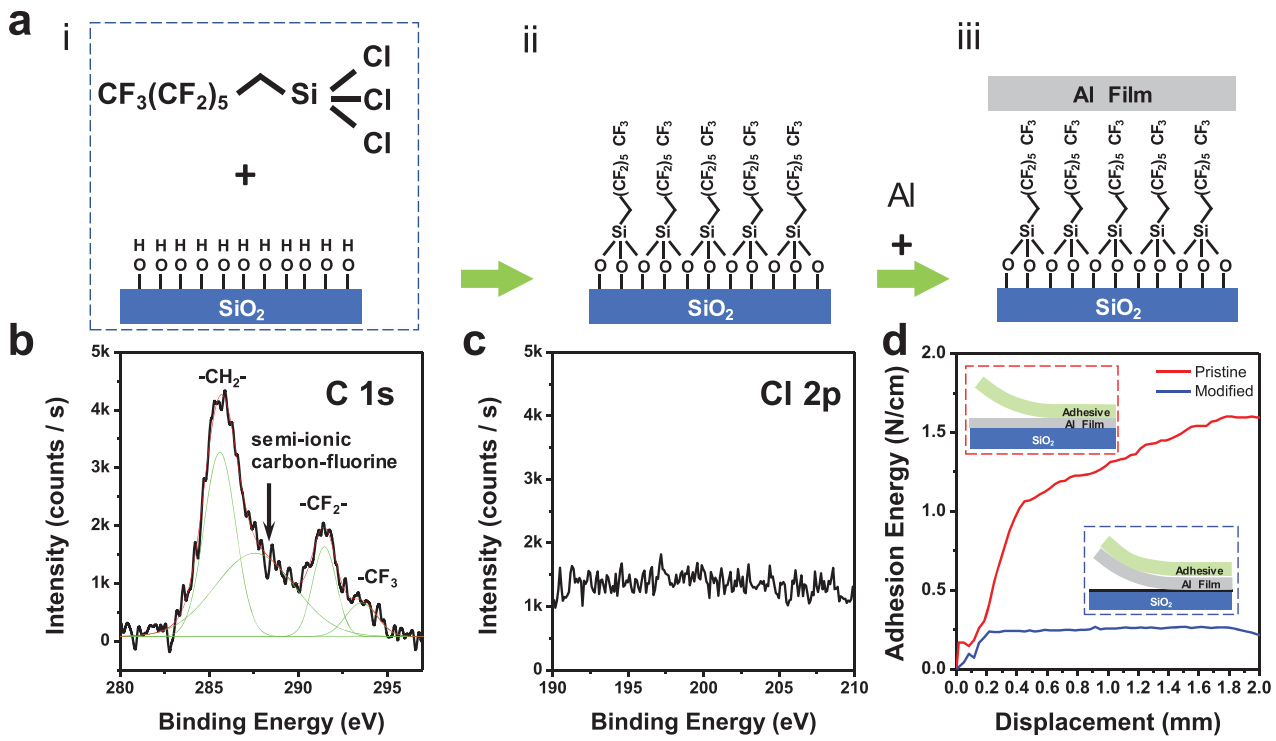

Figure 3. Analysis of surface modification for adhesion engineering of the Al-based SPL process. a) Schematic illustration of the SAM reaction during the modification process. b,c) Measured XPS spectra of the SiO_2/Si substrate after surface modification in the C 1s and Cl 2p binding energy regions. d) Adhesion energy test results of Al film on pristine and modified SiO_2/Si substrates.

polymer, as shown in the inserted dashed red box in Figure 3d. Furthermore, a peeling test was carried out to quantitatively evaluate the peeling of Al film from the two different surfaces. The force–displacement curve in Figure 3d shows that the adhesion energy between the Al film and the modified SiO_2 interface was ≈0.25 N cm^{-1}, while that between the Al film and the pristine substrate was greater than 1.6 N cm^{-1}, leading to stripping of the adhesive polymer from the Al film. It can be safely concluded that the adhesion engineering activated by SAMs enabled the ability to strip Al film from the substrate, which is essential to the SPL process for high-resolution patterning of Al nanostructures.

Enabled by the nanogaps defined by the SPL process, the Fano resonance between Al nanostructures that have been difficult to fabricate in the past can be experimentally achieved. A plasmonic heptamer can support Fano resonance and is observed in Au and Ag nanostructures.[25,26] However, the Fano resonance of the Al heptamer has not been reported because of the comparatively weak plasmon coupling in Al nanostructures as well as the challenge in defining ultrasmall gaps in Al heptamers. The Fano resonance among Al nanostructures is numerically and experimentally investigated in this section. The calculated intensity of the Fano resonance of Al heptamers with different gap sizes is shown in **Figure 4**a. Figure 4a shows that the extinction spectra have an obvious Fano resonance when the gap size in the Al heptamer decreases to sub 20 nm. Regularly arranged Al heptamers were fabricated using the modified SPL method, as shown in Figure 4b. As illustrated in the inset of Figure 4b, the Al nanodisks in the Al heptamer are spaced by HSQ templates, and the gap has a uniform size of ≈12 nm. The exposed HSQ templates are transparent.[27] The red line in Figure 4c is the measured spectrum, with an obvious Fano dip at a wavelength of 1350 nm, which is in accordance with the simulation results, indicated by the blue line. The consistency of the line shape and the wavelengths of the peaks and dip in the measurement and simulation is attributed to the unique nanofabrication fidelity and resolution of the SPL process. To further understand the Fano resonance in the Al heptamer, the charge distributions at the three labeled spectral positions were determined and are presented in Figure 4d. As shown in Figure 4di,iii, which correspond to the charge distributions at wavelengths of 1120 and 1510 nm, respectively, the plasmon polarization oscillated in all seven disks. The in-phase resonance behavior of plasmon resonance in all disks indicates the formation of bright superradiant mode, which exhibits a broad extinction peak due to the large dipole moments. For the charge distribution at the middle dip (spectral position B), the polarization of the plasmon resonance in the central disk is opposite to the plasmon polarization of the ring-like hexamer, which gives rise to the formation of a narrow subradiant mode due to the relatively small dipole moments. The results from Figure 4d confirm that the presence of the Fano dip in the extinction spectrum from the Al heptamer comes from the destructive interference between the broad superradiant mode and a narrow subradiant mode.[28]

The giant electric field confinement enabled by plasmonic nanogaps can enhance the interaction of molecules with light, amplifying the fingerprint vibration of molecular analyzer with low abundance in SERS and SEIRA characterizations.[30–32] Compared to Au or Ag nanostructures, which are commonly

© 2019 WILEY-VCH Verlag GmbH & Co. KGaA, Weinheim

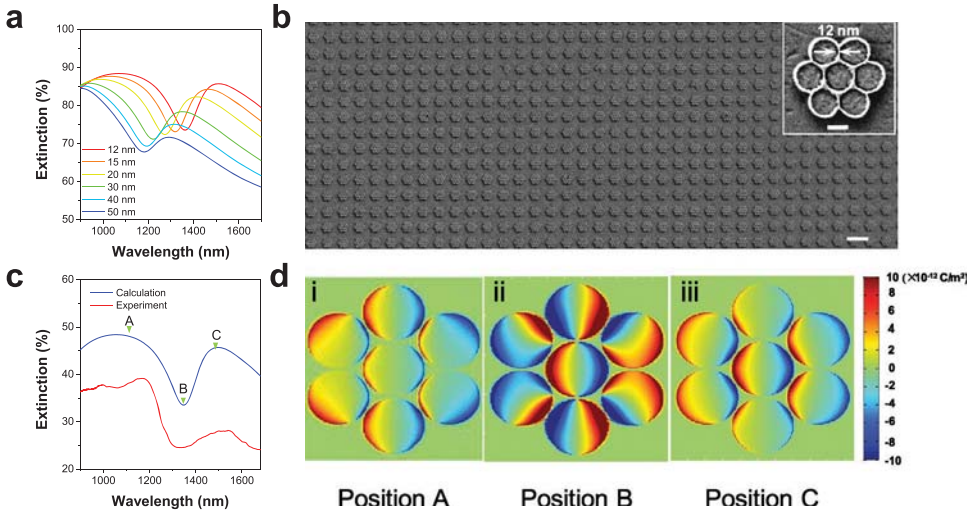

Figure 4. Plasmon-mode analysis of the fabricated Al heptamer. a) Simulated spectra of Al heptamers with different gap sizes. b) Fabricated Al heptamer array with a pitch of 2 µm. In the inset, the enlarged electron micrograph shows that the Al heptamer has uniform interparticle gaps of ≈12 nm. Each disk in the Al heptamer has an identical diameter of ≈270 nm. c) Calculated spectrum (blue) and experimental spectrum (red). The labeled A, B, and C points represent the three spectral positions of 1120, 1348, and 1510 nm in panel (d). d) Analysis of resonance modes based on the charge distribution at the three positions marked in (c). In all simulations, we considered that the HSQ templates remained in nanogaps and were regarded as a dielectric material with a refractive index of 1.4.[29] Scale bar: 2 µm. Inset: 200 nm.

used substrates for SERS and SEIRA, Al nanostructures with tiny gaps are an alternative substrate for chemical sensing applications due to the advantages of low cost and oxidation stability.[33–36]

Bowtie antenna is a commonly used structure for SERS because of the extremely high field enhancement in the corner-to-corner gap.[14] The advantages of the high-resolution multiscale patterning of the SPL process enable us to improve the fidelity in defining such fine features. The resultant Al bowtie nanoantenna array manufactured by employing the Al-based SPL process is shown in **Figure 5**a. According to the overview image, no defects occur for the resultant Al bowtie nanoantenna array in terms of either missing or unwanted residue of Al film. The reliable definition of large-area Al bowtie nanoantennas via the SPL process guarantees a steady SERS performance when using Al nanostructures. The inset in the upper right of Figure 5b shows that an 8 nm gap and a 5 nm curvature of radius for the corner features were precisely achieved in the Al bowtie nanoantenna. A smaller gap size and sharper corners in the Al bowtie nanoantenna enable more efficient concentration of the light field in the plasmonic nanogap. As shown in Figure 5b, the resonance response of the Al bowtie nanoantenna was determined by measuring the single-particle dark-field scattering. The longitudinally polarized spectrum (red line) shows a resonance peak at 556 nm, which is appropriate for SERS excitation by a 532 nm laser. The scattering peak under transverse polarization (perpendicular to the axis of the dimer) blueshifts ≈56 nm compared with the result under longitudinal polarization (parallel to the axis of the dimer). The difference of resonant wavelengths in the experiments and simulations (as shown in Figure S2d, Supporting Information) may be ascribed to the imperfections in fabrication, such as rounded corner features, a trapezoidal profile, and deviation of the optical constant of the deposited Al film. The distinct shifting of the scattering peaks of the longitudinal and transverse excitations indicates the existence of plasmon coupling between Al bowtie antennas. A laser-excited SERS measurement was performed to demonstrate the potential of the Al bowtie nanoantenna for chemical sensing. Crystal violet was used as an analyte to evaluate the SERS performance. In Figure 5c, the Raman-shift signal under longitudinal excitation is more than four times stronger than that under transverse excitation, which is contributed by the greater field enhancement in the corner-to-corner gap, as indicated by the simulations (in Figure S2a–c, Supporting Information).

The fingerprint absorption of molecular vibrational resonance can also be amplified by plasmon resonance in the infrared region. Here, an Al fan-shaped antenna array was employed to enhance the fingerprint absorption from molecules, and the results are shown in Figure 5d. The inset of Figure 5d shows the detailed information of a single fan-shaped antenna, which consists of two partial Al disks with a corner-to-corner nanogap. The small gap of ≈15 nm in the center of the antenna results in a high concentration of the light field in the gap region. Meanwhile, the specific fan shape of the antenna has been verified to have the ability to strengthen the field enhancement in the central gap because of the decreased loss in the rounded ends.[37] As a demonstration, the structured sample coated with a thin PMMA polymer film (≈120 nm) was measured by micro-FTIR reflectance. The serial polarized reflection spectra in Figure 5e consistently confirm the existence of PMMA, as indicated by the formation of a Fano-like dip at 1730 cm^{-1} (corresponding to the C=O bond stretching in the PMMA molecule).[38] A series of reflection micro-FTIR spectra of the Al fan-shaped antennas with different gap sizes resonated at ≈1730 cm^{-1} were measured. As shown in Figure 5f, the enhancement factor as a function of the gap size for the antenna vibrational signals at 1440, 1485, and 1730 cm^{-1} was further studied to quantify the detection performance. The figure shows that the enhancement factors at all three spectral

© 2019 WILEY-VCH Verlag GmbH & Co. KGaA, Weinheim

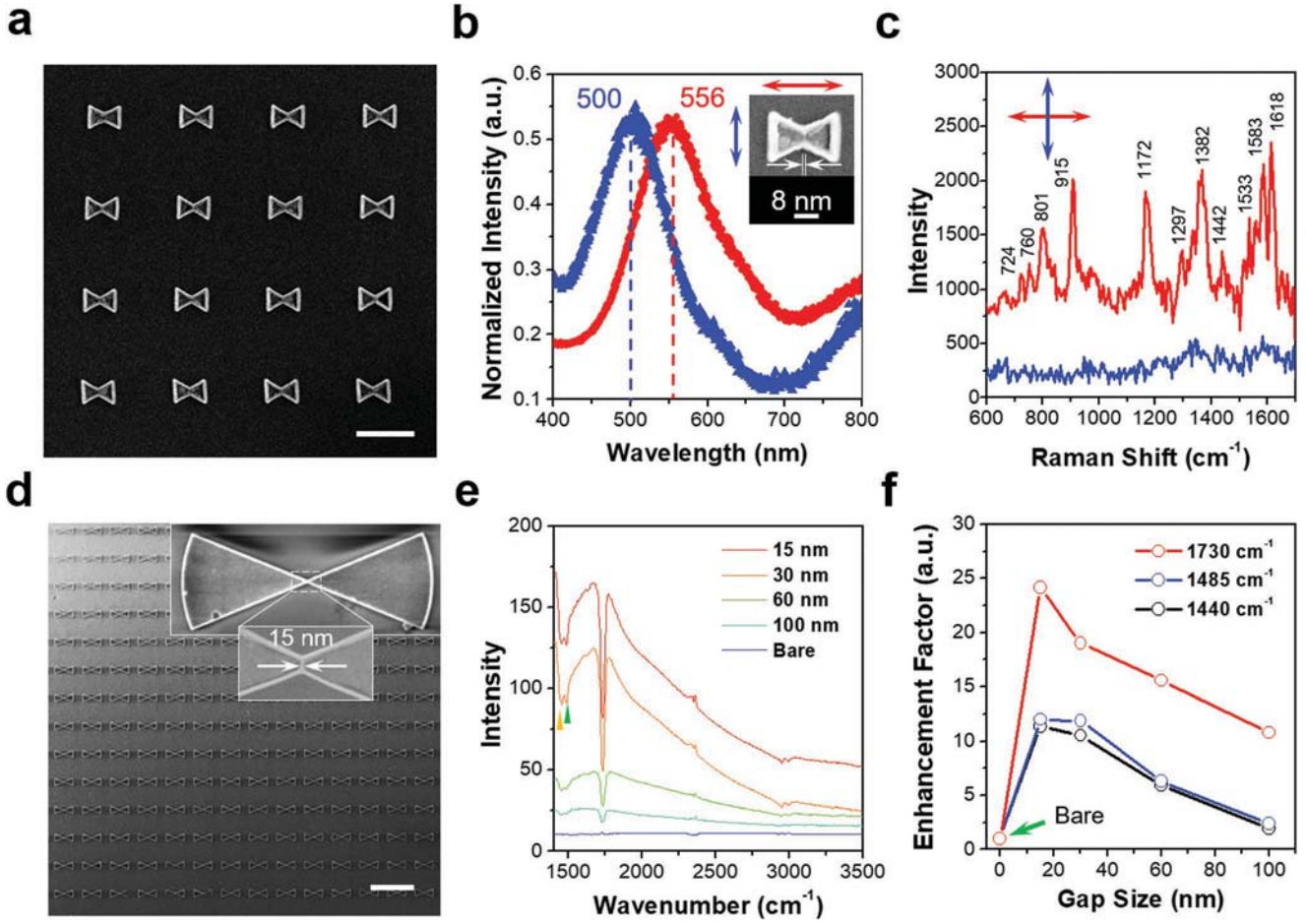

Figure 5. Chemical sensing using Al plasmonic nanogaps. a) Al bowtie array with a pitch of 1 µm. The central gap is ≈8 nm, and the two Al triangles have an edge length of 100 nm. The white lines in each particle present the HSQ outline template. b) Dark-field scattering spectra of the Al bowtie in panel a) under the excitation of longitudinal (red, parallel to the axis of the dimer) and transverse (blue, perpendicular to the axis of the dimer) polarization as labeled in the inset. c) Polarized Raman measurement of the Al bowtie. The crystal violet molecule was used as an analyte for the evaluation of the SERS performance. d) SEM image of a fan-shaped Al antenna array. The inset shows a high-resolution electron micrograph of a single Al antenna. The central gap is ≈15 nm. e) Reflective FTIR spectra of PMMA-coated fan-shaped antenna arrays with different gap sizes. All FTIR spectra refer to the signal of the bare region on the samples. The intensity is the ratio of the reflectance at the structured region to that at the bare region ($I = R_{structure}/R_{bare}$). The marks are used to label the two resonance positions of 1440 cm^{-1} (yellow) and 1485 cm^{-1} (green). f) Plots of the enhancement factor as a function of the gap size at three different vibrational signals of 1440, 1485, and 1730 cm^{-1}. Scale bar: a) 500 nm; (inset in b) 100 nm; d) 10 µm.

positions increase with decreasing gap size. For a given gap size, the higher enhancement factor at 1730 cm^{-1} originates from the energy matching of the plasmon resonance with this specific vibrational signal. To clarify the enhancement mechanism, the extinction spectrum and the field enhancement at the corresponding three spectral positions for a given gap size of 15 nm were also calculated (see Figure S3, Supporting Information). The peak of the strongly coupled dipolar plasmonic resonance at 1724 cm^{-1} is close to the specific vibrational signal of 1730 cm^{-1}, and thus, the intensity of the electric field in the gap at 1730 cm^{-1} is higher than that at the other two positions.

3. Conclusion

In summary, we extended the applicability of the SPL process for Al structures via adhesion engineering, with which Al plasmonic nanogaps approaching to 10 nm scale were achieved with high fidelity. We demonstrated that the nanogaps promote the coupling between Al nanoparticles and benefit the field enhancement in Al plasmonic nanogaps. Fano resonance in the Al heptamer with 12 nm gap was experimentally observed. Enabled by the field enhancement in nanogaps, the chemical sensing based on SERS and SEIRA was performed by the Al bowtie nanostructure and the fan-shaped antenna, respectively. Considering the key role of the nanogaps in plasmonic applications, our work offers a new opportunity to Al plasmonics for various applications such as nonlinear optics and chemical sensing.

4. Experimental Section

Electron Beam Lithography: A hydrogen silsesquioxane (HSQ, XR-1541-006, Dow Corning) resist layer of 100 nm thickness was first spin-coated on the substrate at the speed of 4000 rpm for 1 min. And then, the sample was directly put into electron-beam lithography system

© 2019 WILEY-VCH Verlag GmbH & Co. KGaA, Weinheim

(Raith-150^{Two}) without any thermal treatment to guarantee the property of high resolution. The HSQ resist was exposed by an accelerating voltage of 30 kV and beam current of 280 pA. The exposed samples were immersed into salty developer (1% wt NaOH + 4% wt NaCl aqueous solution) for 60 s at the temperature of 22 °C and rinsed by DI water for 60 s to stop further development. Finally, the wet samples were dipped into IPA solution to avoid the collapse of thin-wall HSQ structures and used a steady nitrogen gas steam to blow-dry the samples.

Metal Deposition: The aluminum film was prepared by thermal evaporation. First, the chamber was prepumped to the pressure of 1×10^{-5} Pa. The working pressure was less than 5×10^{-5} Pa. To optimize surface roughness, a deposition rate of 15 Å s^{-1}. The film thickness was monitored by high-sensitivity quartz crystal microbalance.

Surface Modification: At first, the sample was activated by oxygen plasma treatment to produce hydrophilic siloxyl groups. Subsequently, the sample was placed in Petri dish and then in a dessicator together with a smaller Petri dish containing a few drops of TFOCS. The dessicator was connected to the vacuum pump, and the air was evacuated from dessicator. The process was kept at the pressure of 80 psi for 30 min. During the process, TFOCS vaporize and deposit on the surface of the sample.

Defining Al Structures by Peeling Off: At first, the sample was fixed on a slide glass by pasting Scotch tape on the edges and then curable adhesive polymer was poured (Norland, NOA-61) onto the sample. The adhesive polymer was cured by the illumination of UV light (365 nm, 48 W). When the polymer was completely cured, the blade was used to slowly lift the adhesive polymer layer from the edge of sample and then gently peeled it off using a tweezer till the absolute detachment of polymer layer from the substrate.

X-Ray Photoelectron Spectroscopy: The chemical structure of SAMs was characterized by X-ray photoelectron spectroscopy (PHI 5000C ESCA system) using Al Ka radiation (250 W, 10 kV).

Scanning Electron Microscopy: The morphologic characterization was performed at a field-emission scanning electron microscope (Carl-Zeiss SIGMA HD). Because the optical substrate is insulated, the accelerating voltage was set to be 1 kV and the working distance was kept at 3 mm to obtain high-resolution images.

Optical Measurements: To investigate Fano resonance of Al heptamers, the transmission spectrum measurement was performed in the transmittance mode using 2030PV UV–vis–NIR rang microspectrometer (CRAIC Technology Inc.). The incident light was unpolarized.

The single-particle dark-field scattering spectra of Al nanobowtie were measured in a confocal microscope system (WITec Alpha 300R). The light from a halogen lamp (100 W, 3150 K) was illuminated on the surface of sample through a dark-field module. The white light was filtered by adding a broadband linear polarizer into the incident path. The signal of scattering was collected by an objective (Zeiss Epiplan, 50 ×, N.A. = 0.75) and detected by an electric-cooled CCD (Andor, DV 401-BV-352). All of the measured signals from particle and bare substrate were accumulated with the integration time of 0.5 s for 10 times. The normalized calculation of dark-field scattering was based on the formula as follow

$$I_{scat} = \frac{I_{particle} - I_{substrate}}{I_{halogen} - I_{dark}} \quad (1)$$

where $I_{scat}(\lambda)$ presented the real scattering signal from single gold nanostructure; the spectrum of $I_{particle}$, $I_{substrate}$, was separately measured from the original particle and adjacent substrate. $I_{halogen}$, I_{dark} was the spectrum of light source and background count of measurement system, respectively.

Surface-Enhanced Raman Scattering: First, the sample structured by Al nanobowties was decorated with a layer of crystal violet molecules by an immersion process. The SERS measurement was performed on the confocal microscope. The Raman signal excited by 532 nm laser is collected by 100× objective (ZEISS Epiplan, N.A. = 0.9) and detected by a spectrometer equipped with E-cooled CCD camera. The extraction of Raman signal was set to the integration time of 2 s for three times.

Micro-FTIR Measurement: Reflectance spectra of PMMA-capped Al Fan-shaped antennas arrays were performed on an infrared microscopy system (Nicolet in10) combined with Fourier-transform spectrometer possessing the wavenumber resolution of 8 cm^{-1}. The efficiency of micro-FTIR measurement was strengthened by a Cassegrain objective (15×, N.A. = 0.4). Meanwhile, an aperture (200 μm × 200 μm) was used to improve signal-to-noise ratio. The reflective signal was obtained by a liquid N_2-cooled MCT photodetector.

FDTD Simulation: The simulation of electric-field and charge distribution was calculated by a commercial software (FDTD solution 8.0 version, Lumerical Solution Inc.). Accurate modeling was referred to the size of structures from SEM images. Corresponding to the measured spectrum from structure array, the periodic boundary condition was set in *X* and *Y* axes and perfect-matched layer was used in *z* axis. For the simulation of dark-field scattering from single particle, the boundary condition of perfect-matched layer in three dimensions were performed in calculation domain. A fine mesh was added in domain and the size was set to be 2 nm in *XY* plane and 3 nm in *Z* direction. The complex dielectric constants for Al and SiO_2 were selected as CRC and Palik database, respectively. The optical property of exposed HSQ resist was set to 1.4 as a dielectric material.

Supporting Information

Supporting Information is available from the Wiley Online Library or from the author.

Acknowledgements

This work was supported by National Natural Science Foundation of China (Grants Nos. 51722503, 51621004, 51805160, and 11574078). The authors are grateful to Mr. Enming You from Xiamen University for the Micro-FTIR measurement.

Conflict of Interest

The authors declare no conflict of interest.

Keywords

adhesion engineering, aluminum plasmonics, plasmonic nanogaps, “Sketch and Peel” lithography, surface-enhanced spectroscopy

Received: July 17, 2019
Revised: October 14, 2019
Published online: November 6, 2019

[1] D.-K. Lim, K.-S. Jeon, H. M. Kim, J.-M. Nam, Y. D. Suh, *Nat. Mater.* **2010**, *9*, 60.
[2] P. H. C. Camargo, M. Rycenga, L. Au, Y. Xia, *Angew. Chem., Int. Ed.* **2009**, *48*, 2180.
[3] D.-K. Lim, K.-S. Jeon, J.-H. Hwang, H. Kim, S. Kwon, Y. D. Suh, J.-M. Nam, *Nat. Nanotechnol.* **2011**, *6*, 452.
[4] H. Im, K. C. Bantz, N. C. Lindquist, C. L. Haynes, S.-H. Oh, *Nano Lett.* **2010**, *10*, 2231.
[5] D. R. Ward, F. Hüser, F. Pauly, J. C. Cuevas, D. Natelson, *Nat. Nanotechnol.* **2010**, *5*, 732.
[6] S. F. Tan, L. Wu, J. K. W. Yang, P. Bai, M. Bosman, C. A. Nijhuis, *Science* **2014**, *343*, 1496.

© 2019 WILEY-VCH Verlag GmbH & Co. KGaA, Weinheim

[7] M. Celebrano, X. Wu, M. Baselli, S. Großmann, P. Biagioni, A. Locatelli, C. De Angelis, G. Cerullo, R. Osellame, B. Hecht, L. Duò, F. Ciccacci, M. Finazzi, *Nat. Nanotechnol.* **2015**, *10*, 412.
[8] M. Kauranen, A. V. Zayats, *Nat. Photonics* **2012**, *6*, 737.
[9] D. C. Marinica, A. K. Kazansky, P. Nordlander, J. Aizpurua, A. G. Borisov, *Nano Lett.* **2012**, *12*, 1333.
[10] Y. Wu, C. Zhang, N. M. Estakhri, Y. Zhao, J. Kim, M. Zhang, X.-X. Liu, G. K. Pribil, A. Alù, C.-K. Shih, X. Li, *Adv. Mater.* **2014**, *26*, 6106.
[11] M. W. Knight, N. S. King, L. Liu, H. O. Everitt, P. Nordlander, N. J. Halas, *ACS Nano* **2014**, *8*, 834.
[12] M. W. Knight, L. Liu, Y. Wang, L. Brown, S. Mukherjee, N. S. King, H. O. Everitt, P. Nordlander, N. J. Halas, *Nano Lett.* **2012**, *12*, 6000.
[13] H. Duan, H. Hu, K. Kumar, Z. Shen, J. K. W. Yang, *ACS Nano* **2011**, *5*, 7593.
[14] H. Duan, A. I. Fernández-Domínguez, M. Bosman, S. A. Maier, J. K. W. Yang, *Nano Lett.* **2012**, *12*, 1683.
[15] Y. Chen, Q. Xiang, Z. Li, Y. Wang, Y. Meng, H. Duan, *Nano Lett.* **2016**, *16*, 3253.
[16] Y. Chen, K. Bi, Q. Wang, M. Zheng, Q. Liu, Y. Han, J. Yang, S. Chang, G. Zhang, H. Duan, *ACS Nano* **2016**, *10*, 11228.
[17] Q. Chen, C. Martin, D. R. S. Cumming, *Plasmonics* **2012**, *7*, 755.
[18] H. Duan, K. K. Berggren, *Nano Lett.* **2010**, *10*, 3710.
[19] N. Verellen, Y. Sonnefraud, H. Sobhani, F. Hao, V. V. Moshchalkov, P. V. Dorpe, P. Nordlander, S. A. Maier, *Nano Lett.* **2009**, *9*, 1663.
[20] S. Zhang, G.-C. Li, Y. Chen, X. Zhu, S.-D. Liu, D. Y. Lei, H. Duan, *ACS Nano* **2016**, *10*, 11105.
[21] A. Kuzyk, Y. Yang, X. Duan, S. Stoll, A. O. Govorov, H. Sugiyama, M. Endo, N. Liu, *Nat. Commun.* **2016**, *7*, 10591.
[22] D. Qin, Y. Xia, G. M. Whitesides, *Nat. Protoc.* **2010**, *5*, 491.
[23] J. A. DeRose, E. Hoque, B. Bhushan, H. J. Mathieu, *Surf. Sci.* **2008**, *602*, 1360.
[24] I. Palchan, M. Crespin, H. Estrade-Szwarckopf, B. Rousseau, *Chem. Phys. Lett.* **1989**, *157*, 321.
[25] J. A. Fan, C. Wu, K. Bao, J. Bao, R. Bardhan, N. J. Halas, V. N. Manoharan, P. Nordlander, G. Shvets, F. Capasso, *Science* **2010**, *328*, 1135.
[26] K. Thyagarajan, J. Butet, O. J. F. Martin, *Nano Lett.* **2013**, *13*, 1847.
[27] D. L. Olynick, B. Cord, A. Schipotinin, D. F. Ogletree, P. J. Schuck, *J. Vac. Sci. Technol., B: Nanotechnol. Microelectron.: Mater., Process., Meas., Phenom.* **2010**, *28*, 581.
[28] M. Hentschel, M. Saliba, R. Vogelgesang, H. Giessen, A. P. Alivisatos, N. Liu, *Nano Lett.* **2010**, *10*, 2721.
[29] D. Dregely, F. Neubrech, H. Duan, R. Vogelgesang, H. Giessen, *Nat. Commun.* **2013**, *4*, 2237.
[30] A. J. Haes, C. L. Haynes, A. D. McFarland, G. C. Schatz, R. P. Van Duyne, S. Zou, *MRS Bull.* **2005**, *30*, 368.
[31] R. Stanley, *Nat. Photonics* **2012**, *6*, 409.
[32] S. Lal, N. K. Grady, J. Kundu, C. S. Levin, J. B. Lassiter, N. J. Halas, *Chem. Soc. Rev.* **2008**, *37*, 898.
[33] N. S. King, L. Liu, X. Yang, B. Cerjan, H. O. Everitt, P. Nordlander, N. J. Halas, *ACS Nano* **2015**, *9*, 10628.
[34] B. Cerjan, X. Yang, P. Nordlander, N. J. Halas, *ACS Photonics* **2016**, *3*, 354.
[35] S. Tian, O. Neumann, M. J. McClain, X. Yang, L. Zhou, C. Zhang, P. Nordlander, N. J. Halas, *Nano Lett.* **2017**, *17*, 5071.
[36] C. J. DeSantis, M. J. McClain, N. J. Halas, *ACS Nano* **2016**, *10*, 9772.
[37] L. V. Brown, X. Yang, K. Zhao, B. Y. Zheng, P. Nordlander, N. J. Halas, *Nano Lett.* **2015**, *15*, 1272.
[38] A. Braun, S. A. Maier, *ACS Sens.* **2016**, *1*, 1155.

 © 2019 WILEY-VCH Verlag GmbH & Co. KGaA, Weinheim